Colloids and Surfaces A: Physicochemical and Engineering Aspects 641 (2022) 128522

Contents lists available at ScienceDirect

Colloids and Surfaces A: Physicochemical and Engineering Aspects

journal homepage: www.elsevier.com/locate/colsurfa

# Improved hybrid-shelled perfluorocarbon microdroplets as ultrasound- and laser-activated phase-change platform

D. Palmieri [a,1], F. Brasili [b,c,1], A. Capocefalo [b,c], T. Bizien [d], I. Angelini [a], L. Oddo [a], Y. Toumia [a], G. Paradossi [a], F. Domenici [a,*]

[a] Department of Chemical Sciences and Technologies, University of Rome Tor Vergata, Rome, Italy
[b] Department of Physics, Sapienza University of Rome, Rome, Italy
[c] Institute for Complex Systems (ISC-CNR), National Research Council, Rome, Italy
[d] Synchrotron SOLEIL, L'Orme des Merisiers, Saint-Aubin, France

## HIGHLIGHTS

- Novel hybrid-shelled microdroplets as dual-responsive phase-change contrast agents.
- The microdroplets combine good colloidal stability with chemical versatility.
- Acoustic droplet vaporisation yields stable and echogenic microbubbles.
- Gold nanoparticles decoration unlocks laser triggered microdroplet vaporisation.
- This multimodal platform is promising for imaging and theranostics.

## GRAPHICAL ABSTRACT

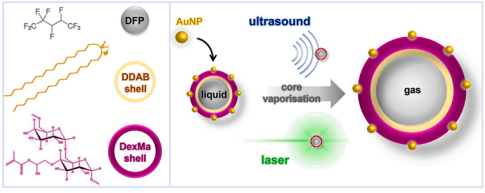


## ARTICLE INFO

*Keywords:*
Microdroplets
Acoustic Droplet Vaporisation
Optical Droplet Vaporisation
Dextran shell
Gold nanoparticles

## ABSTRACT

*Hypothesis:* We propose significant improvements to perfluorocarbon microdroplets, conferring them colloidal stability, chemical versatility, and size control. Decafluoropentane cores are stabilized by biocompatible interfaces – either a monolayer of the cationic surfactant dimethyldioctadecylammonium bromide (DDAB) or a double shell obtained by adding crosslinked dextran methacrylate as further coating – and functionalised with gold nanoparticles. We hypothesize that this formulation enables dual, acoustic (ADV) and optical (ODV) vaporisation of microdroplets into microbubbles, yielding a versatile "phase-change" theranostic platform.
*Experiments:* Microdroplets synthesis is optimized by high-speed homogenization methodology. Functionalisation with gold nanoparticles is achieved by electrostatic decoration. The colloidal suspension is characterised by the concerted use of dynamic light scattering, electrophoresis, and confocal microscopy, to assess microdroplets' stability. Additional structural details are provided by small-angle X-ray scattering. We analysed the ultrasound- and laser-stimulated transition into microbubbles and characterised their response to ultrasound by acoustic spectroscopy.
*Findings:* Hybrid-shelled microdroplets were produced at high density, with narrow diameter distribution (~1 μm). The highly charged surface and the long hydrocarbon tails of DDAB protruding within the core provide high stability. The elastomeric dextran layer at the water interface allows obtaining stable cavitating microbubbles by

* Corresponding author.
[1] These authors contributed equally to this work

https://doi.org/10.1016/j.colsurfa.2022.128522
Received 25 November 2021; Received in revised form 1 February 2022; Accepted 3 February 2022
Available online 7 February 2022

ADV exhibiting interesting viscoelastic features. The presence of gold nanoparticles unlocks the opto-thermal microdroplet vaporisation.

## 1. Introduction

Microdroplets (MDs) with a liquid perfluorocarbon (PFC) core exposed to either an ultrasound field or an optical stimulus can transform into microbubbles (MBs) by the processes known as Acoustic (ADV) or Optical Droplet Vaporisation (ODV), respectively [1–7]. Thanks to the acoustic response of the MBs formed after vaporisation, MDs represent "phase-change" ultrasound or photoacoustic contrast agents suitable for enhancing the imaging contrast of pathological areas or even for tracking at high frame rate the dynamics in blood flows [5–9]. Recent literature has also shown that droplet vaporisation could be exploited in various medical treatments, mainly focused on the vascular system, to boost targeted drug delivery [10–12]. The possibility of combining the enhanced echogenicity after vaporisation with the capability of transporting therapeutics represents the main asset of MDs and makes them promising theranostic agents [1,13].

In this respect, the two key features involved in both diagnostic and therapeutic efficacy are the size distribution and the composition of the stabilising shell. For *in vivo* use, the smallest MDs size achievable is desirable in order to reach the thinner capillaries, whose typical lumen is 5–10 μm, without causing their occlusion. Despite several MDs formulations have been proposed in recent years, a synthesis protocol that accomplishes this requirement and produces MDs with good yield is still lacking to date [4,7,14,15].

The stabilising shell is directly involved in the bonding with the carried agents (*e.g.,* drugs or functional nanoparticles) and in the targeting towards specific tissues [16,17], it could affect the vaporisation efficiency, and it determines the acoustic response of the MBs formed after vaporisation [18–21]. On top of these, the primary role of the shell lies in ensuring the stability and the size uniformity of MDs over time. This is essential to ensure the possibility of performing highly contrasted and localised echographic imaging of tissues using acoustic fields with extremely low intensity, thus minimising the risk of mechanical and biological damages to healthy cells associated with the exposure to ultrasound frequencies of medical relevance [22,23]. The MDs shell can be made up of lipid, protein or polymer [24]. MDs with lipid or protein shells efficiently vaporise into highly echogenic MBs, that nonetheless have a short shelf-life [24,25]. Polymer shelled MDs are more stable and offer high chemical versatility for modification with ligands [26], drugs or other active agents, although their echogenicity and vaporisation efficiency are generally poor for PFCs with boiling point exceeding the body temperature [24].

In this frame, we focused our efforts in establishing optimal synthesis protocol and shell composition of MDs, including their functionalisation with gold nanoparticles (AuNPs). We dealt with the latter task to exploit the peculiar interaction of AuNPs with visible light, that is characterised by the resonant absorption at the so-called Localised Surface Plasmon Resonance (LSPR) [27–29] with consequent thermal release of the stored energy, called thermoplasmonic effect. This phenomenon, combined with the good biocompatibility of AuNPs [30], has been exploited to promote ODV [3,4,31–34], to induce the photoacoustic effect [5,35,36], and to support photothermal therapies [37,38], also *in vivo*.

In previous work, we developed and modelled novel phase change contrast agents based on a PFC core stabilised by a double shell, with an internal monolayer composed by Epikuron™200, a mixture of surfactants with slightly negative charge, and an external layer made of crosslinked chains of biocompatible and biodegradable polysaccharides, dextran or hyaluronic acid, grafted with a methacrylic moiety [16]. The surfactant monolayer plays a key role in this synthesis protocol, in fact its amphiphilic properties allow to interface the hydrophilic polymer with the hydrophobic core of the MDs and therefore promotes the formation of the external layer of the shell [16]. Such shells provide interesting properties to the system. In particular, the robustness and the viscoelastic features of the polymeric methacryloyl-grafted dextran (DexMA) layer allow for the reversibility of the ADV process, with MBs relaxing back to the MDs state after ultrasound switching off [26]. Nevertheless, there are still some drawbacks in the synthesis procedure to overcome. Specifically, the MDs average diameter of several microns is too large for the actual deployment *in vivo*, and the high polydispersity results, upon ADV, in the formation of MBs with non-uniform acoustic properties.

Moving from these results, here we exploit the information provided by several light scattering, microscopic, and acoustic methodologies to improve the synthesis of surfactant-DexMA-shelled MDs, with specific focus on the shell. We vary the emulsification parameters such as time and speed, with the aim of reducing the size and the polydispersity of MDs. Moreover, in order to improve the colloidal stability and the vaporisation efficiency of the system, the composition of the internal monolayer is modified using the biomedical relevant gel-crystalline surfactant Dioctadecyldimethylammonium bromide (DDAB). Its long acyl chains lead to better stability, while the marked positive charge provides on one hand a good colloidal stability even to MDs encapsulated only by the surfactant monolayer. On the other hand, in the perspective of employing our platforms for the delivery of therapeutics, it favours the loading of negatively charged compounds, such as nanoparticles, drugs molecules or nucleic acids for gene therapy, and promotes the interaction with the cell plasma membrane. For these reasons, DDAB is widely employed to date to realise vectors for targeted gene and drug delivery approaches [13,39–41]. We exploit the electrostatic interactions to decorate MDs with anionic AuNPs, whose presence opens to the possibility of optically improving the vaporisation efficiency. Both ADV and ODV processes are assayed in detail on the different types of MDs synthesised.

## 2. Materials and methods

### 2.1. Materials

Dextran (molecular weight 35–40 kDa) from *Leuconostoc mesenteroides*, palmitic acid (PA), 1,1,1,2,3,4,4,5,5,5-decafluoropentane (DFP, boiling temperature 55 °C), DDAB, pyrene, fluorescein isothiocyanate (FITC), dimethylsulfoxide (DMSO), 4-(Dimethylamino)-pyridine, glycidyl methacrylate, hydrochloric acid, Nile red and acetone are Sigma-Aldrich (Milan, IT) products. Epikuron™200 was purchased from Cargill Texturizing Solutions GmbH & Co. (Hamburg, DE). 2-Hydroxy-1-[4-(2-hydroxyethoxy) phenyl]- 2-methyl-1-propanone, Irgacure® 2959, is purchased from BASF (Kaisten, CH). Chloroform is purchased from Carlo Erba Reagents (Milan, IT). Ultrapure water (18.2 MΩ·cm at 25 °C) was produced by a deionisation apparatus from PureLab (Perugia, IT). Dialysis tubes, cut off 12–14 kDa, purified as standard procedure, were Medicell International Ltd (London, UK) product. Citrate-coated AuNPs with nominal diameter of 60 nm and number density of $2.6 \times 10^{10}$ $mL^{-1}$ were purchased from Ted Pella Inc. (Redding, CA, US).

### 2.2. Synthesis of the surfactant and surfactant-DexMA shelled MDs

The surfactant- and surfactant-DexMA-shelled MDs were prepared by the two-step method sketched in Fig. 1, that is based on the protocol previously reported in literature [16,26].

In the first step of the procedure (panel A), a surfactant (DDAB or Epikuron™200) monolayer was deposited around the DFP droplets by an oil-in-water emulsion. This step is essential to allow the deposition of

the hydrophilic polymer onto the droplet in the second step of the procedure and therefore to enable the formation of the external layer of the shell. In fact, preliminary synthesis tests demonstrated, in accordance with literature [16], that DFP droplets stabilised only by a DexMA shell do not form. To deposit the monolayer, we mixed 500 μL of DFP with 600 μL of 10 mM surfactant solution in ethanol and 8.6 mL of water. The emulsification was then performed for 3 min using an UltraTurrax T25 (IKA, DE). As will be described in the Results and Discussion section, the emulsification velocity $v$ is one of the parameters we studied to optimise the MDs diameter distribution. Surfactant-shelled MDs were thus obtained by adding 3 mL of MilliQ water without interrupting the emulsification. After 3 min the emulsification was stopped, and the resulting mixture was washed by centrifuge (5 min at 164 RCF). The pH of the resulting dispersion was 7.2 as measured by pH-Meter Basic 20 + (Crison, ES).

In the second step (panel B) the surfactant-DexMA-shelled MDs were obtained by deposition of a DexMA layer at the water/surfactant interface of the MDs. The detailed description and a scheme of the reaction used to produce DexMA with degree of substitution of 50%, are reported in section S1 of ESI. 3 mL of 20 mg/mL DexMA aqueous solution was added drop by drop without interrupting the emulsification, which was further kept going for a time $\tau$, the other parameter we investigated to optimise MDs synthesis. Afterwards, the mixture was centrifuged for 5 min at 164 RCF to separate the formed surfactant-DexMA-shelled MDs from excess DexMA. Once the supernatant containing the non-deposited DexMA was removed, MDs were redispersed in 3.6 mg/mL solution of Irgacure® 2959 photoinitiator in water. To crosslink the vinyl sidechains of DexMA, the dispersion was cured by UV exposure for 4 min under continuous and gentle stirring, using a B-100 A (Black Ray, US) equipped with a 365 nm light source operating at 7 mW/cm$^2$ (Ted Pella, US). We measured the pH of the resulting dispersion to 7.5. The successful formation of the MDs and the deposition of the DexMa layer were ascertained by Confocal Laser Scanning microscopy (CLSM, see Section 2.4 for details). To this aim we labelled DFP core by Nile red and DexMA by FITC. To label the MDs hydrophobic core, in the first step Nile red was added to liquid DFP at the concentration of 31 μM. To label the DexMA external shell, 10 μL of FITC solution (5 mg/mL in DMSO) were added to 2 mL of MDs suspension and left react in the dark for 1 h under 200 RPM stirring. Then the suspension was centrifuged at 164 RCF for 5 min to remove the excess FITC, and labelled MDs were redispersed in 2 mL of water. Centrifuging was repeated until the supernatant appeared transparent by eyes. The number density of the produced MDs was measured by microscopy, as described in Section 2.4.

A third step was added to the protocol to decorate MDs with AuNPs (panel C of Fig. 1). The decoration of the external shell (both surfactant and surfactant-DexMA types) was obtained by electrostatic adsorption of AuNPs: 1 mL of AuNPs stock solution (2.6 $\times 10^{10}$ mL$^{-1}$ in water) was added to 2 mL of MDs solution (1.8 $\times 10^{8}$ mL$^{-1}$ in water) and stirred for 5 min at 200 RPM. The solution was then centrifuged at 164 RCF for 5 min to remove non-conjugated AuNPs and the pellet containing MDs was re-dispersed in water to the final volume of 2 mL. The number density of AuNPs-decorated MDs in the final sample was measured by microscopy.

### 2.3. Dynamic light scattering

To estimate particles' size, we used the hydrodynamic diameter as measured by Dynamic Light Scattering (DLS). Therefore, in the following we refer to this quantity as the size or the diameter of particles. Experiments were performed using a Hamamatsu HC120 photometer (Brookhaven Instruments, NY, US), equipped with a BI-200SM goniometer, a BI-9000 AT photocorrelator, a solid-state laser (Suwtech. Inc., SHA, CN) with wavelength of 532 nm powered by a power supply LDC-2500 (Suwtech. Inc.) and a phototube (Hamamatsu Photonics K.K., JP). For measurements, samples were placed in a quartz cuvette and the temperature was controlled using an external F30-C thermostat (Julabo GmbH, DE) circulating water in a coil placed in the vat containing the refractive index matching liquid. Except for the analyses of thermal stability and for ODV experiments, we kept the sample temperature at 25 °C during measurements. The acquisition time of each measurement was set to 2 min, suitable to achieve on the one hand a statistically relevant number of counts and on the other hand to avoid artefacts due to sample stratification (*e.g.*, MDs sedimentation or floating up of MBs). In this respect, we considered the acquisition time appropriate if it was

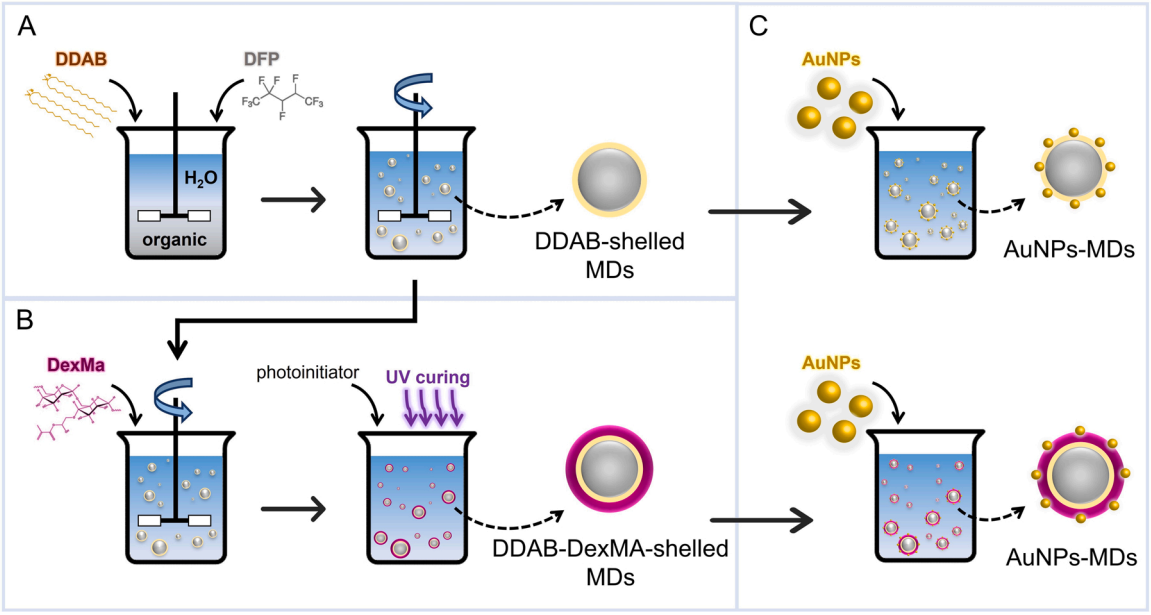


**Fig. 1.** Scheme of the MDs fabrication protocol. Surfactant-shelled MDs are obtained by emulsification of a mixture of DFP, surfactant and water (A). Surfactant-DexMA-shelled MDs were obtained by adding a DexMA solution to the surfactant-shelled MDs dispersion, agitating the sample for 5 min and centrifuging to remove non-adsorbed DexMA; afterward a photoinitiator was added to the dispersion, and a UV curing procedure led to the polymer crosslinking (B). For both the shell types, AuNPs-decorated MDs were obtained by adding the AuNPs solution to MDs; after 5 min stirring, non-adsorbed AuNPs were removed by centrifugation (C).

possible to acquire at least three consecutive stable measurements and afterwards to obtain the same size distribution by measuring the same sample after agitation. We also successfully compared hydrodynamic diameter distributions with diameter distributions obtained by CLSM (see section S3 of ESI).

Measurements were repeated at least three times for each sample. To obtain intensity distributions of hydrodynamic diameter according to the Stokes-Einstein equation, the measured autocorrelation functions were analysed using the CONTIN algorithm of the Dynamic Light Scattering Software ver. 3.18 (Brookheven Instruments). A Gaussian fitting procedure was applied to size distributions using the OriginPro 8.1 software. Size values reported in this work are the average ± standard deviation over the different diameter values (at least three) of the distribution centre obtained on the same sample. The distributions shown in the figures are normalised to the maximum intensity value.

### 2.4. Optical and confocal laser scanning microscopy

Microscopy images were acquired by using an inverted microscope Eclipse Ti-E (Nikon Co., Tokyo, JP) equipped with a sCMOS Andor Zyla 4.3 camera (Andor Instruments, Belfast, UK). The images herein reported were acquired using objectives (Nikon, Florence, IT) with magnification, 60 × (oil immersion, numerical aperture 1.4, Plan APO), 40× and 20×.

For CLSM we used the multi-excitation module mechanism of the microscope, equipped with a Ar-ion (Spectra Physics, CA, US), 454–676 nm wavelength, and a He-Ne (Melles Griot, CA, US), 543.5 nm wavelength, laser sources. The 60× oil immersion objective was used for imaging. Image deconvolution was performed by Nikon NIS-Elements software version 5.40.00, using the Richardson-Lucy algorithm with 20 iterations.

All the samples were monitored using a motorised stage and the frames' acquisition was performed by Nikon NIS-Elements AR Analysis software version 4.3. Z-stacks of images were acquired, according to Nyquist criterion, with 0.15 μm increments, automatically calculated by the Nikon EZ-C1 acquisition software. The 3D reconstruction of samples was performed using the NIS Elements AR Analysis software.

MDs diameter distributions were determined using the Nikon software EZ-C1. MDs number density was measured by using a Neubauer cell counting chamber (BRAND, Wertheim, DE) with the 40× objective and the counting method was adopted for MDs. For each sample we measured at least 4 frames; values are reported as average ± standard deviation.

### 2.5. Differential scanning calorimetry

For differential scanning calorimetry (DSC) measurements we employed a DSCQ-200 instrument (TA Instruments Inc., Milan, IT), equipped with an RCS-90 cooling system. A Tzero sample press kit (TA Instruments Inc.) was used to close aluminium Tzero hermetic crucibles, placed on the instrument housings, one filled with the sample and the second used as a reference. Thermograms were recorded under a nitrogen atmosphere with a flow rate of 50 mL/min, with temperature scanning at 1 °C/min after 5 min of equilibration at the starting temperature of 25 °C. To get the temperature and transition enthalpies we analysed the thermograms with the Universal Analysis 2000 software ver.4.5 A (TA Instruments Inc.) and OriginPro 8.1 software.

### 2.6. ζ-potential

ζ-potential was measured at 25 °C using a NanoZetaSizer apparatus (Malvern Instruments LTD, Worcester, UK), equipped with a 5 mW He-Ne laser. The electrophoretic mobility $\mu_e$ of samples was measured by combining laser Doppler velocimetry and phase analysis light scattering. Measured values were converted into the ζ-potential distributions using the Smoluchowski relation:

$$\zeta = \frac{\mu_e \eta}{\varepsilon} \quad (1)$$

where $\varepsilon$ and $\eta$ are the solvent permittivity and viscosity, respectively.

### 2.7. UV-Visible extinction spectroscopy

UV-Visible extinction spectra were recorded using a V-630 spectrophotometer (Jasco, Tokyo, JP) equipped with a deuterium-halogen lamp and a Peltier thermostatted holder EHC-716 (Jasco). The spectral resolution is of 1 nm. Experiments were performed at 25 °C; for temperature trends, after every temperature change the samples were kept thermalising for 10 min before acquisition. To measure the LSPR wavelength of AuNPs, a Gaussian fitting was performed in the resonant absorption region of the spectra. The reported values are the average and standard deviation on at least three independent spectra. All the analyses carried out on the extinction spectra were performed using the OriginPro software, version 8.1.

### 2.8. Small angle X-ray scattering

Small Angle X-ray Scattering (SAXS) measurements were performed at the SWING beamline of Synchrotron SOLEIL (Saint Aubin, France). The sample-to-detector distance was 6.5 m. Scattering patterns were recorded with a two-dimensional EigerX 4-M detector (Dectris, Baden, Switzerland) at 12 keV, allowing measurements in the q-range from 0.001 to 0.18 $Å^{-1}$. The q-vector is defined as $q = (4\pi/\lambda) \sin\theta$, where $2\theta$ is the scattering angle. The investigated samples were diluted to the MDs number density of $1.0 \times 10^6 mL^{-1}$ and filled in capillaries with a diameter of 1.5 mm. Exposure time of 1 s was used for acquisitions. Scattering patterns of an empty capillary and of a capillary filled with Milli-Q water were recorded for intensity background subtraction. Data processing of the recorded 2D images and averaging were performed by the image analysis software Foxtrot (SOLEIL software group and SWING beamline).

The scattered intensity *I(q)* from a collection of particles can be expressed in terms of the particle form factor *P(q)* and of the system structure factor *S(q)*, according to the equation:

$$I(q) = nv^2 \Delta\rho^2 P(q) S(q) \quad (2)$$

where $\Delta\rho$ is the contrast in electron density between sample and solvent, $n$ is the number density of scattering particles and $v$ their volume. The form factor *P(q)* describes the ensemble averaged shape of scattering objects in solution whereas the structure factor *S(q)* accounts for the interference introduced by interparticle correlations. At the concentration employed for the experiments, MDs dispersed in solution can be reasonably treated as non-interacting, hence $S(q) \approx 1$ and only the form factor contributes to the scattering profile. Data analysis was performed by SasView software version 5.0 [42].

### 2.9. Acoustic droplet vaporisation

For ADV experiments we used a SP100 (Sonidel, Dublin, IE) sonoporator, equipped with an unfocussed ultrasound transducer with effective radiating area of 0.8 $cm^2$. Continuous ultrasound waves with central frequency of 1 MHz and nominal intensity in the range 0.5–3.6 $W/cm^2$ were applied to the samples. The acoustic contact was assured by a plastic half-funnel filled with ~3 $cm^3$ of gel (PBpharma, Turin, IT) for medical sonography. Sample solutions (15 mL, $\sim 10^8 mL^{-1}$ MDs number density) were placed in a Falcon tube and, before irradiation, thermalised using a RCT basic heater (IKA®-Werke, Staufen, GE) and an ETS-D5 electronic contact thermometer (IKA®-Werke). We tested different thermalising temperature, acoustic intensities, and irradiation times (see section S5 of ESI) to select the most performing experimental conditions.

We calibrated the acoustic intensity by directly measuring the ultrasound field inside the Falcon tube used for ADV with a needle hydrophone of 0.5 mm diameter (Precision Acoustics, UK). During calibration the setup configuration was exactly the same used for ADV experiments. The calibration of peak negative pressure and intensity is reported in section S2 of ESI. Intensity values are provided in terms of spatial peak temporal average intensity, *i.e.*, the maximum spatial intensity measured when the pulse is activated, averaged over the period of oscillations, and therefore we refer to this quantity as the acoustic intensity.

Upon ADV transition, MBs tend to rise up to the water surface due to the lower density of the vapour core. To visualise the MBs by CLSM, 7 μL were taken from the surface of the dispersion immediately after switching off the ultrasound field and rapidly placed on a glass slide. For frame acquisition, we adjusted the focal plane as close as possible to the upper interface with the glass slide where most MBs are placed. We estimated a delay of approximately 1 min between turning off the ultrasound field and the frame acquisition.

The vaporisation yield was estimated by the ratio between the number density of completely vaporised microbubbles and that of MDs in the sample before irradiation.

### 2.10. Optical droplet vaporisation

For ODV experiments we used the laser (Suwtech. Inc.) of the DLS instrument, emitting at 532 nm. This wavelength was chosen to match the LSPR of the AuNPs and therefore to maximise the thermal energy released after irradiation due to the thermoplasmonic effect. To induce the vaporisation of MDs, samples were irradiated with intensity of 34 mW/cm$^2$ for different times, varying between 60 and 300 s. The laser intensity was calibrated as reported in section S2 of ESI. After ODV, diameter distributions were measured by DLS and analysed by OriginPro 8.1 software. During irradiation, the sample temperature was kept constant at 37 °C using the thermostat of the DLS apparatus.

For CLSM, 7 μL were taken from the surface of the dispersion immediately after switching off the laser and rapidly placed on a glass slide. For frame acquisition, we adjusted the focal plane as close as possible to the upper interface with the glass slide where most MBs are placed. We estimated a delay of approximately 1 min between turning off the ultrasound field and the frame acquisition.

### 2.11. Acoustic attenuation spectroscopy

The MBs obtained by vaporisation of MDs were characterised by acquiring their acoustic attenuation spectra in aqueous environment. The experimental set-up employed consists of a quartz cell featuring two parallel open sides separated by a distance of 2 cm, where emitting and receiving flat 10 MHz transducers V311-SU (Olympus Co, MA, US) are located. The sample chamber was filled with 18 mL of MDs solution (number density $n_{MB}$ ~$10^8$ mL$^{-1}$) and acoustic spectra were acquired immediately after ADV.

The signal of each sample detected by the receiver was analysed by comparing it to those obtained on Milli-Q water and on non-vaporised MDs as reference samples. The amplitude fundamental of water medium was set to 0.4 V. The apparatus was controlled by LabView Transmission software (National Instruments, Austin, TX, US).

The acquired spectra are framed in a linear oscillation model, in terms of a resonance frequency $\omega_{res}$ and a viscous damping coefficient $\delta$, which depend on the viscoelastic properties of the oscillating MBs shell [18]. Moreover, if MBs in the analysed samples show narrow size distribution sufficiently stable over time, it is possible to assume that they have all the same radius $R$ [19]. The expression for the attenuation coefficient $\alpha(\Omega)$ as a function of the normalised frequency $\Omega = \omega/\omega_{res}$ is then given by the equation:

$$\alpha(\Omega) = 4\pi R^2 n_{MB} \frac{c\delta}{R\omega_{res}} \frac{\Omega^2}{\left(1-\Omega^2\right)^2 + \delta^2\Omega^2} \quad (3)$$

where $c$ is the speed of sound in the liquid. A fitting procedure is performed on each spectrum by gnuplot software version 5.2 to extrapolate the MBs resonance frequency and the damping coefficient.

## 2. Results and discussion

In this section we report the study aimed at developing two different types (surfactant- and surfactant-DexMA-shelled MDs) of phase change contrast agents, consisting in MDs with a hydrophobic liquid core, whose shells provide improved physical properties suitable for medical application. In the first part, we describe the optimisation of the synthesis of the MDs in terms of diameter distribution and shell surface charge. In the second part, we propose a simple strategy, based on electrostatic adsorption, for functionalising the surfactant-DexMA shell of MDs shell with AuNPs. We carefully characterised the proposed systems and studied their ageing and stability with respect to temperature. In the last part, we focused on the acoustic and optical vaporisation of MDs, with the aim of providing novel, hybrid phase change contrast agents for combined diagnosis and therapy applications.

### 2.1. Improved synthesis of MDs

We performed a thorough study of the MDs preparation in terms of parameters of emulsification in water and composition of the shell. Two types of MDs, surfactant- and surfactant-DexMA-shelled, were prepared referring to the method sketched in Fig. 1 and described in Section 2.2. Briefly, a surfactant layer was deposited around DFP droplets by emulsification (with velocity $\nu$ and time $\tau$ as parameters). For MDs with an external elastomeric shell, this step was followed by the further deposition of a DexMA layer and by the crosslinking of polymer chains by free radical polymerisation.

Representative DLS analysis of average values $d$ and standard deviations $\Delta d$ of the diameter distributions of Epikuron™200-DexMA-shelled MDs in water at varying the emulsification parameters $\nu$ and $\tau$ are reported in Table 1. It shows an empirical size trend, increasing with $\nu$, up to 16,000 RPM. Afterwards, for higher velocity, the size decreases. This behaviour can be explained in terms of two competing processes: the breaking of MDs, and their coalescence, which are both favoured when increasing $\nu$ [43]. This could mean that when $\nu$ moves from 8000 to 16,000 RPM, coalescence of DFP MDs is predominant. As expected, the turbulent hydrodynamic regime, modulated by $\nu$, strongly influences the size polydispersity of the MDs. Polydispersity is a fundamental feature, since the acoustic properties of the MBs obtained upon vaporisation strictly depend on their size, which is in turn related to the initial diameter of the MDs [44]. Hence, a population characterised by low

**Table 1**
DLS study of the diameter $d$ of MDs with Epikuron™200-DexMA shell as a function of the emulsification velocity $\nu$ (with $\tau$ fixed at 60 s, on the left) and of the emulsification time $\tau$ (with v fixed at 13000 RPM, on the right). The value $\tau = 0$ means that the emulsification was stopped immediately after adding the last drop of DexMA solution (second step of the synthesis protocol). The values corresponding to the minimum of the relative width $\Delta d/d$ of the diameter distribution, selected as optimum, are highlighted in bold. Emulsification times leading to doubled diameter distribution are labelled by * .

| $\nu$ (RPM) | $d$ (μm) | $\Delta d/d$ | $\tau$(s) | $d$ (μm) | $\Delta d/d$ |
|---|---|---|---|---|---|
| 8000 | 0.3 ± 0.2 | 6.7 × 10$^{-1}$ | 0 | 1.0 ± 0.2 | 2.0 × 10$^{-1}$ |
| 10000 | 0.5 ± 0.4 | 8.0 × 10$^{-1}$ | 30 | 0.8 ± 0.1 | 1.3 × 10$^{-1}$ |
| **13000** | **1.3 ± 0.1** | **7.7 × 10$^{-2}$** | **60** | **1.3 ± 0.1** | **7.7 × 10$^{-2}$** |
| 16000 | 2.3 ± 1.0 | 4.3 × 10$^{-1}$ | 300 * | 0.2 ± 0.1 | 5.0 × 10$^{-1}$ |
| | | | | 1.9 ± 0.5 | 2.6 × 10$^{-1}$ |
| 20000 | 1.0 ± 0.4 | 4.0 × 10$^{-1}$ | 600 * | 0.2 ± 0.1 | 5.0 × 10$^{-1}$ |
| | | | | 6.0 ± 2.5 | 4.2 × 10$^{-1}$ |

polydispersity yields ultrasound contrast agents with uniform resonance frequency. The relative width $\Delta d/d$ of the distribution has a minimum for $\nu = 13{,}000$ RPM, corresponding to a MDs average diameter of 1.3 μm. A diameter of ~1 μm is well-suited for reaching, when injected, the smallest capillaries without inducing their obstruction, even in applications that involve the vaporisation of MDs. For these reasons we selected $\nu = 13{,}000$ RPM as optimum value for the emulsification velocity.

Table 1 also shows that the size slightly depends on $\tau$ up to 60s, while for longer emulsification times coalescence becomes predominant and the MDs formulations show bimodal diameter distributions. In the range of $\tau$ where the diameter has unimodal distribution, the relative width $\Delta d/d$ of the distribution decreases with $\tau$. For the same reasons exposed above, we selected $\tau = 60$ s as optimum value, yielding the more monodisperse distribution centred around 1.3 μm.

The resulting marked improvement of the MDs size features is shown in Fig. 2 in comparison with literature [26]. In particular, the diameter distribution (panel A) appears considerably narrowed and centred at a value 4 times lower than that previously achieved. In panel B, we show a representative CLSM image of MDs whose liquid core is labelled with the solvatochromic fluorophore Nile red. Due to the property of the dye to show very intense red fluorescence when placed in hydrophobic environment, the image demonstrates that DFP is actually encapsulated in the MDs core.

With the aim of further improving the shell stability and increasing the affinity to anionic AuNPs, we introduced DDAB, a cationic surfactant characterised by a long apolar tail, as novel component of the internal surfactant shell to replace Epikuron™200, which consisted in a heterogeneous mixture of surfactants with low negative charge and short or medium hydrophobic chains. In this way we expect an improved colloidal stability of MDs due to the higher surface charge ensured by DDAB: it has been indeed reported that high ζ-potential values, related to high charge density in the electro-chemical double layer surrounding MDs, hinder coalescence [45]. To this aim, we progressively varied the composition of the surfactant layer in both types of MDs, surfactant- and surfactant-DexMA-shelled. We used mixtures of DDAB and Epikuron™200 with increasing fraction of DDAB in the first step of the synthesis protocol (Fig. 1, panel A) and characterised the obtained systems by microscopy and DLS measurements. The measured number density, ζ-potential and diameter of MDs are reported in Fig. 3 as a function of the DDAB fraction in the surfactant.

The number density of MDs shows a significant increase when the fraction of DDAB exceeds 0.5: from $1.1 \pm 0.1 \times 10^8 mL^{-1}$ to $2.6 \pm 0.3 \times 10^8 mL^{-1}$ for MDs with surfactant-shell, and from $1.0 \pm 0.1 \times 10^8 mL^{-1}$ to $2.0 \pm 0.2 \times 10^8 mL^{-1}$ with surfactant-DexMA-shell (Fig. 1, panel A). This highlights a dramatic increase in the yield of the preparation protocol related to the presence of DDAB. A slightly higher yield is observed in the case of MDs stabilised only by the surfactant layer, mainly at the higher DDAB fractions. ζ-potential measurements also show a clearly increasing trend for both MDs types (Fig. 1, panel B). This result assesses the actual progressive replacement of Epikuron™200 in the surfactant shell. The lower variation of ζ -potential measured in the case of surfactant-DexMA-shelled MDs is due to the shielding effect of the outer polymeric layer. Moreover, experiments highlight that in both cases the diameter distribution does not depend on the composition of the surfactant shell, remaining at constant values around 1.3 μm (Fig. 3, panel C). This points out that the optimised emulsification parameters remain preserved when Epikuron™200 is replaced by DDAB. In general, these results highlight the marked stabilising role of DDAB that leads to a doubled MDs production yield.

In fact, the change in the composition of the surfactant shell significantly enhances the surface charge of MDs, resulting in a strong electrostatic repulsion that improves their colloidal stability and hinders coalescence. Consistently, this effect is more marked in the surfactant-shelled MDs, whose surface charge is not shielded by the DexMA layer. Another effect of stabilisation could be due to the long aliphatic chains of DDAB, that deeply penetrate the hydrophobic core of the droplet [46,47]. Moreover, as compared to Epikuron™200, that is a mixture of different surfactant chains, DDAB can organise in a more homogeneous gel-crystalline phase [48,49] at the MDs interface, increasing the shell stiffness. Consistently, this effect emerges with the marked jump in the yield occurring when DDAB becomes the main component of the shell, *i.e.* at fractions higher than 0.5. Based on the highlighted yield enhancement of about two-fold and on the suggested stability improvement associated to the increasing amount of DDAB, we proceed our analyses using inner surfactant shells composed only by DDAB.

To ascertain the successful deposition of the DexMA layer on the MDs with the selected surfactant composition, we prepared samples using FITC-labelled DexMA in the shell and Nile red in the core. Representative CLSM images and 3D reconstructions are reported in section S3 of ESI, confirming that DexMA is actually deposited around the droplet core. The analyses of size distribution performed on MDs with the selected surfactant composition are also reported in section S3 of ESI for both DDAB and DDAB-DexMA shells. In Fig. 4, we analyse MDs ageing in terms of number density and diameter distribution. We studied both the shell types and reported for comparison the study performed on Epikuron™200-DexMA-shelled MDs. MDs were kept at room temperature throughout the whole duration of the experiment. In all cases, the MDs number density has a decreasing trend (Fig. 4, panel A). This effect appears to markedly slowdown in DDAB-DexMA-shelled MDs with respect to the Epikuron™200-DexMA-shelled ones. Specifically, Epikuron™200-DexMA-shelled MDs are completely vanished after 6 days, while the number density of DDAB-DexMA-shelled MDs decreases to

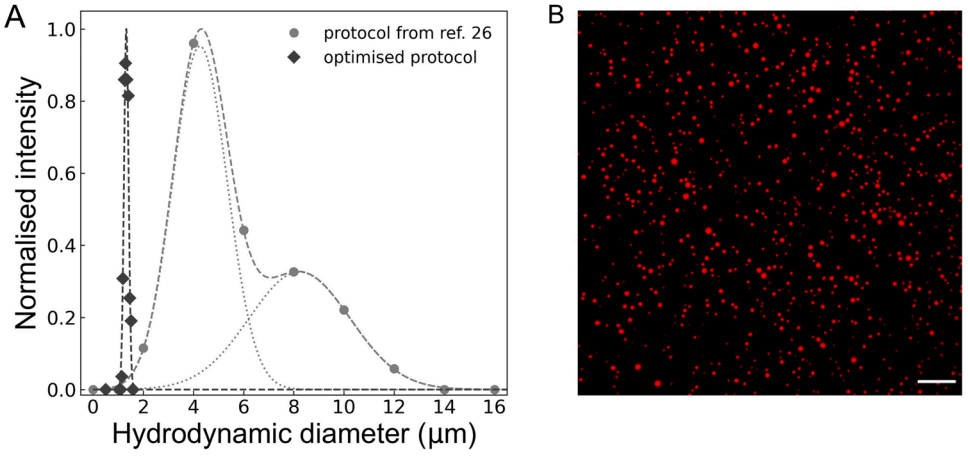


**Fig. 2.** Characterisation of the new formulation of DFP MDs with double-layer shell. (A) Comparison between hydrodynamic diameter distributions of the optimised preparation (dark grey) and of the preparation previously reported in ref. 26 (light grey); full marks represent the measured distributions, dashed lines the Gaussian best fits, and dotted lines are the two components of the fitting curve. (B) Representative CLSM image of MDs synthesised with the optimised protocol, where the DFP core is labelled by Nile red; the scalebar is 10 μm. (For interpretation of the references to colour in this figure, the reader is referred to the web version of this article.)

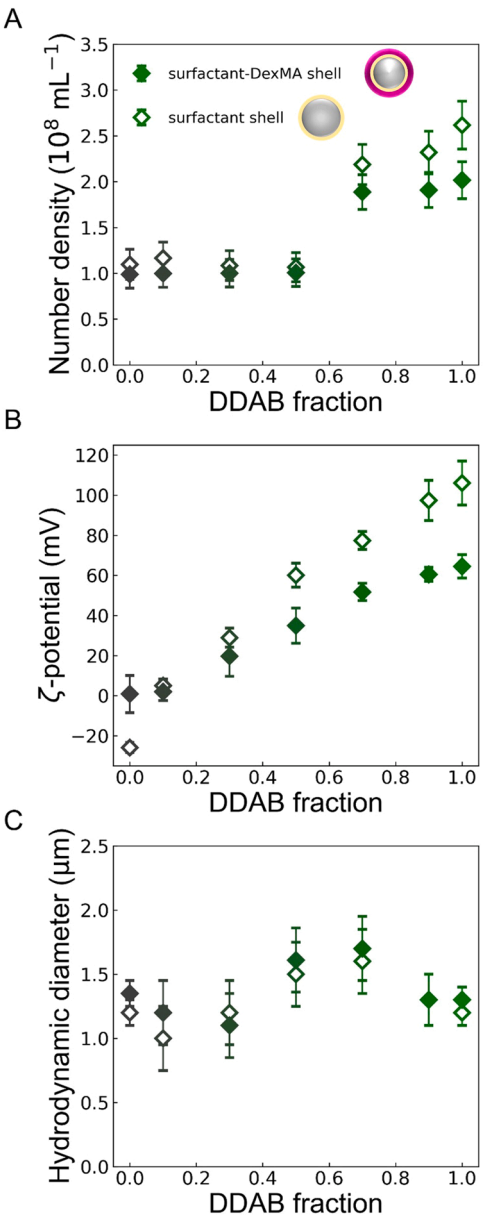


**Fig. 3.** Characterisation of MDs synthesised with varying composition of the surfactant layer. Measurements of number density (A), ζ-potential (B) and hydrodynamic diameter (C), as a function of the DDAB fraction employed in the synthesis protocol of surfactant-DexMA-shelled (full diamonds) and surfactant-shelled (empty diamonds) MDs. In panel A, each point and error bar of the plot represents the average value and the standard deviation evaluated on at least four CLSM frames.

~20% in two weeks. In the case of DDAB-shelled MDs, the number density trend is substantially superimposed to that of DDAB-DexMA-shelled MDs during the first ageing week. Afterwards, during the second week, the reduction in the number of DDAB-shelled MDs appears faster. Diameter measurements (panel B) highlight for all the MDs types a marked widening of the distributions and an increase of the average value when the number of MDs falls below 10% of the initial amount. This enlightens the role of coalescence in the ageing process of the bubbly suspension.

The ageing analyses on one hand ascertain the key role of the electrostatic repulsion between MDs colloids in preventing coalescence and hence in markedly enhancing their shelf-life. Specifically, a significant portion of the DDAB-shelled MDs hold intact even after one week, comparably to the typical shelf-life of surfactant-shelled MDs of similar

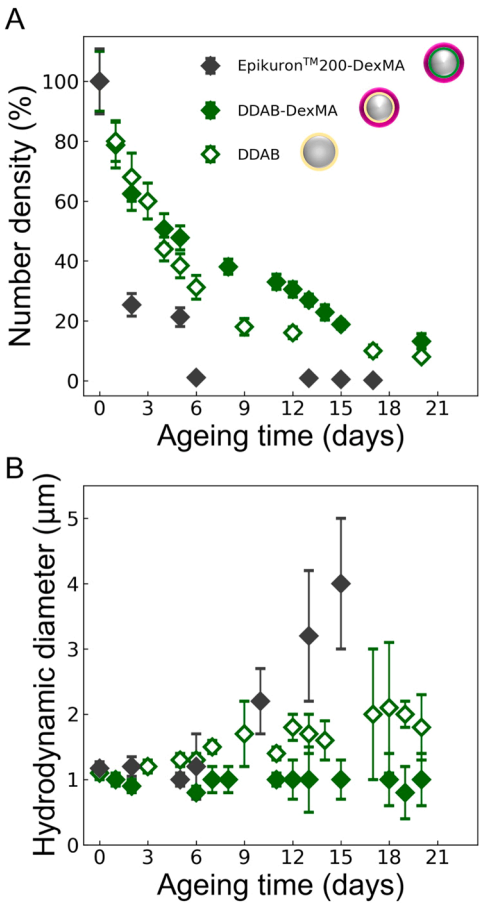


**Fig. 4.** Study of MDs ageing. Temporal evolution of the number density (A), reported as percent of the initial value, and hydrodynamic diameter (B) for DDAB-DexMA-shelled (green full diamonds), Epikuron™200-DexMA-shelled (grey full diamonds) and DDAB-shelled (green empty diamonds) MDs. (For interpretation of the references to colour in this figure, the reader is referred to the web version of this article.)

size [50], making this system interesting for drug delivery applications [13,51]. On the other hand, the results remark the importance of the external.

crosslinked DexMA shell, which provides further stability to the system, contributing to preventing coalescence and avoiding droplets burst. Both advantages are due to the fundamental step of crosslinking that results in the formation of an elastomeric, yet robust, layer.

We also studied the thermal stability of MDs by DLS and DSC measurements, as reported in section S3 of ESI. Both DDAB- and DDAB-DexMA-shelled systems showed good robustness up to the DDAB transition temperature, measured at 46 ± 2 °C consistently with literature [49]. This guarantees their reliability at physiological temperature.

### 2.2. Functionalisation of MDs with AuNPs

AuNPs-decorated MDs were synthesised according to Section 2.2 by electrostatic adsorption of anionic, citrate-coated AuNPs to the positively charged surface of MDs. To benefit of an efficient thermoplasmonic effect, we used AuNPs with a nominal diameter of 60 nm, that have a higher absorption cross section than smaller AuNPs [52]. Moreover, they are non-toxic, differently from AuNPs with lower diameter [53]. The obtained hybrid systems have a diameter of 1.1 ± 0.1 μm and a number density of $3.6 \times 10^7$mL$^{-1}$ in the case of DDAB shells, while in the case of DDAB-DexMA shells the diameter is 1.2 ± 0.1 μm and the number density is $4.7 \times 10^7$mL$^{-1}$.

The adsorption of AuNPs onto the surface of MDs was investigated by

SAXS. The curves obtained at 25 °C on AuNPs-decorated MDs for both the shell types are reported in Fig. 5, in comparison with the corresponding non-decorated systems. The scattering curves of non-decorated MDs, reported and discussed in section S4 of ESI, are consistent with those of hollow spheres with external radius of 604 ± 4 nm in the case of DDAB shell and 585 ± 5 nm in the case of DDAB-DexMA shells (polydispersity of 0.18 and 0.11, respectively) and thickness of the polymeric layer of 355 ± 2 nm (polydispersity of 0.35), as obtained by a fitting procedure based on a standard core-shell sphere model [54]. Such values are in good accordance with the hydrodynamic diameter distributions and with atomic force microscopy measurements previously reported [26]. The disappearing of the scattering curves at 50 °C is consistent with the transition of DDAB at ~ 46 °C and the consequent MDs rupture. In the curves of AuNPs-decorated MDs, the presence of AuNPs in the sample is clearly evident in the characteristic oscillation of the sphere form factor [54] convoluted with the MDs signal. Since non-adsorbed AuNPs were removed from the solution by a centrifuging procedure, this result demonstrates the adsorption of AuNPs on the MDs surface. To investigate in detail the spatial organisation of adsorbed AuNPs, the MDs contribution was removed by subtracting the scattering curves acquired on non-decorated samples. The deconvoluted curves, reported in the insets of Fig. 5, are well fitted by a sphere model form factor, yielding in both cases an average radius of 28.5 ± 0.5 nm, consistent with that obtained on the AuNPs stock solution (Fig. S10). The plateau trend in the low-q region ($q < 0.006$ Å$^{-1}$) points out that AuNPs do not aggregate upon adsorption to MDs and the absence of a structure factor, highlighted in Fig. S11, points out that no short-range correlation can be recognised in their positions, hence adsorbed AuNPs are well separated and randomly distributed onto the droplets surface. In this respect, we estimated by UV-Visible extinction spectroscopy the average number of AuNPs adsorbed to each MD to $x_{ads} = 161 \pm 7$ for DDAB-DexMA shells and $x_{ads} = 209 \pm 8$ for DDAB-shells (Fig. S12), corresponding to 9% and 13% coverage of the MDs surface, respectively.

We analyse the stability of AuNPs-decorated MDs in section S4 of ESI, pointing out that, in the case of DDAB shell, the droplet stability is markedly reduced as compared to their non-decorated counterpart. In the case of DDAB-DexMA shell, a better stability is observed, although also in this case the MDs robustness suffers from the presence of AuNPs. It is plausible that the interaction between the AuNPs and the shell of MDs could perturb their structural stability. In particular, the interaction with the DDAB shell may modify its packing (*i.e.*, fluidification and penetration of water molecules) [55]. It is also worth noting that the negative charge carried by the AuNPs adsorbed to the shell can partially shield the electrostatic repulsion among positively charged MDs. On the other hand, it has been reported [56] that a low-coverage of AuNPs could lead to droplet-droplet bridging, *via* charge patches interactions [57], and thus favour coalescence. Nevertheless, neither rupture nor aggregation of the MDs are induced immediately after adsorption of AuNPs. Therefore, the reduced stability could be more likely attributed to modifications in the DDAB shell packing. Whether the amount of AuNPs is sufficient to boost the efficiency of MDs vaporisation *via* ultrasound or optical irradiation is the subject of our investigation reported in the following section.

### 2.3. Acoustic and optical droplet vaporisation

We study the MDs vaporisation induced by both acoustic and optical stimulus. We first focus on the ADV of non-decorated MDs, both with DDAB- and DDAB-DexMA-shells, to analyse the role of the stabilising shell. The preliminary analyses at varying the intensity of the applied ultrasound, the exposure time, and the temperature of the environment aimed at selecting a set of parameters that led to a significant vaporisation yield in the case of DDAB-DexMA-shelled MBs are summarised in section S5 of ESI. The most relevant results were obtained irradiating MDs for 5 min with intensity of 520 mW/cm$^2$ at 37 °C (120 kPa peak negative pressure, mechanical index 0.12, acoustic dose 156 J/cm$^2$), which is considered safe for biomedical applications [22]. In these conditions we measured a vaporisation yield of 11% ± 3%. The same exposure conditions led to significant but less efficient ADV of DDAB-shelled MDs, with yield of 3.2% ± 0.6%, which is more than three times lower with respect to the DDAB-DexMA shelled MDs.

We first notice that, although the ADV yield could be further improved through a fine tuning of the exposure conditions, it is relevant that MBs production seems strictly dependent on the shell type. This highlights the crucial role of the DexMA layer in preserving the stability of MBs after ADV. Secondly, we note that both types of MDs undergo ADV at the same exposure conditions, even if with different yield. Based on this observation, we hypothesise that the rigidity of the two shell layers involved in our systems are not high enough to have significantly affect the ADV threshold. In fact, according to literature, the ADV process is initiated by the formation of a small bubble into the liquid MD core, whose successful expansion depends on the compressibility of the gaseous phase, liquid inertia, heat transfer, and mechanical properties of the stabilising shell [58–61]. The latter contribution is mainly due to the rigidity of the shell that acts against the expansion of the gaseous phase; hence it is more relevant when the particle size is close to its maximum, *i.e.*, when the core is already vaporised [61]. The presence of the viscoelastic shell mainly affects the growth rate of the nascent bubble [61], while effects on the ADV threshold have been reported to occur only for extremely rigid shells, with shear modulus Gs from several tens to hundreds of MPa [60,61].

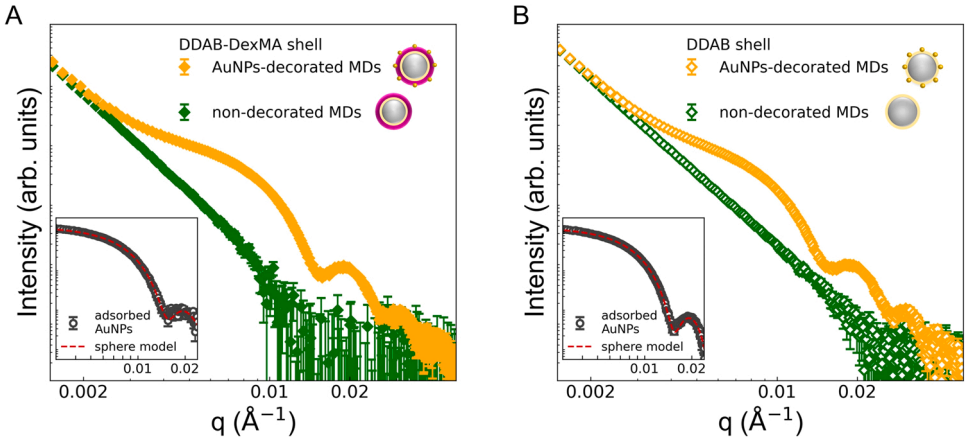


**Fig. 5.** SAXS curves obtained at 25 °C on AuNPs-decorated MDs with DDAB-DexMA (A) and DDAB (B) shell, in comparison with the corresponding non-decorated systems; in the insets: the contribution of adsorbed AuNPs, deconvoluted from that of MDs.

We studied ADV by DLS and CLSM; representative DLS and CLSM results are reported in Fig. 6. Diameter distributions, before and after acoustic irradiation, are shown in panels A and B for DDAB-DexMA- and DDAB-shelled MDs, respectively. In both cases, the samples exposed to acoustic stimulus are characterised by two size populations. The one centred at higher diameter values ($8.8 \pm 0.5$ μm for DDAB-DexMA-shelled MDs and $8.4 \pm 0.9$ μm for DDAB-shelled ones) can be attributed to vaporised MBs. In fact, these diameter values are 8-fold larger with respect to non-irradiated MDs, meaning that the volume of the core expands well above the critical molar volume of DFP [62], thus elastic and Laplace forces exerted by the two layers of the shell on the gas core are not sufficient to induce the recondensation of the MBs into MDs. The second diameter distribution, observed at the same values of non-irradiated samples, can be attributed to MDs whose core did not undergo the transition to the gaseous phase or collapses back to the liquid state after irradiation (*e.g.*, if it does not reach the critical volume [26]).

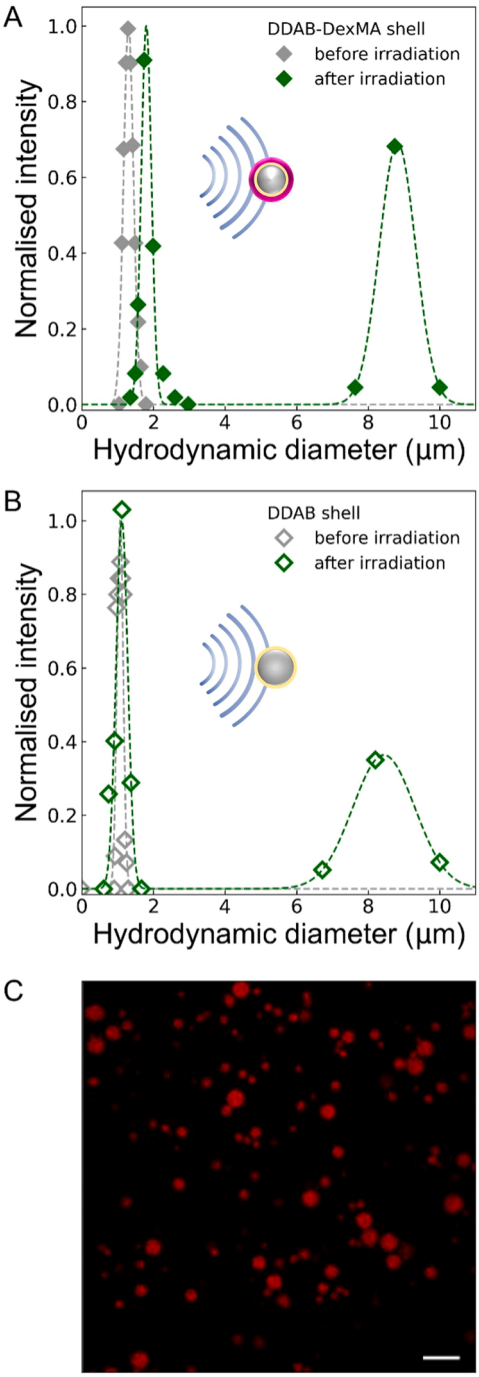


**Fig. 6.** DLS and CLSM study of the ADV process. Hydrodynamic diameter distributions (full marks) and corresponding Gaussian best fits (dashed lines) for DDAB-DexMA- (A) and DDAB- (B) shelled MDs before (light grey) and after (green) acoustic irradiation and representative CLSM image of vaporised MDs with DDAB-DexMA shell (C). The ADV process was induced by irradiating MDs for 5 min with an acoustic field of 520 mW/cm$^2$ intensity at 37 °C. Scalebar is 10 μm. (For interpretation of the references to colour in this figure, the reader is referred to the web version of this article.)

The formation of MBs in the sonicated sample is confirmed by CLSM images acquired before and after irradiation of MDs whose core was previously labelled with Nile red (a representative image of the DDAB-DexMA-shelled sample is reported in panel C). In fact, a significant presence of larger particles, quite compatible with the DLS distribution of Fig. 6A, mainly located close to the top interface with the glass slide, is observed. This is due to the volume expansion and consequent density lowering of the core upon ADV. We deepened the CLSM analysis by extrapolating the diameter distribution from images (Fig. S16), that confirms the appearance of a population of MBs, and by discussing the differences in the MBs diameter distribution with respect to DLS in Section S5 of ESI. The dimmed fluorescence of Nile red is due to the liquid-gas transition of DFP and to the lowered concentration of the dye as a consequence of the increased volume of the core. We imaged samples for at least 10 min, during which the size and the number of MBs remained stable. The appearance of fluorescent areas outside the MBs volume, that could indicate possible leak of DFP during the vaporisation process, was not observed. This suggests that significant damages of the shell do not occur throughout the vaporisation process.

Comparing the diameter distributions after irradiation of MDs with the two types of shell, we note that the size distribution of completely vaporised MBs is more uniform and pronounced in the case of DDAB-DexMA with respect to DDAB. This is consistent with the higher yield of MBs in the case of double-layered shells and can be explained by the stabilising role of the external elastomeric layer, that significantly reduces the leaking of DFP and MBs rupture probability during ADV. This would mean that DDAB-DexMA-shelled MDs may be well-suited for ultrasound contrast imaging purposes. Conversely, the acoustically stimulated destruction of DDAB-shelled MDs may be useful to trigger the release *in situ* of small drug molecules encapsulated in the core to prevent their premature clearance.

We also characterised the acoustic properties of vaporised MDs by acoustic attenuation spectroscopy in section S5 of ESI. The acoustic spectra are fitted to the linear oscillations model of Eq. 3 and the obtained acoustic parameters are further analysed to extrapolate viscoelastic properties of the two layers of the MDs shell. To this aim, we used a thin-shell model [63] for the DDAB shell and thick-shell model [19] for the DDAB-DexMA shell. The results obtained by such analyses are reported in Table 2. The shear modulus $G_s$ and viscosity $\mu_s$ of the DexMA layer are in good accordance with those previously reported for similar systems [19,26]. Notice that $G_s$ is at least one order of magnitude lower than the typical shear modulus values needed to significantly affect the ADV threshold according to the literature [60,61]. This result supports our hypothesis that the shell does not resist expansion with significant strength during the core vaporisation and only intervenes in determining the final size and the stability of the formed MBs (*e.g.*, the thick

**Table 2**
Acoustic and viscoelastic parameters extrapolated by the analysis of the acoustic attenuation spectra of vaporised MDs with both types of shell.

| type of shell | $\omega_{res}$ (MHz) | $\delta$ | $\chi$ (N/m) | $G_s$ (MPa) | $\mu_s$ (mPa·s) |
|---|---|---|---|---|---|
| **DDAB** | $14.8 \pm 0.1$ | $0.95 \pm 0.02$ | $3.7 \pm 0.8$ | – | – |
| **DDAB-DexMA** | $15.5 \pm 0.3$ | $0.4 \pm 0.1$ | – | $3.0 \pm 0.7$ | $100 \pm 30$ |

polymer layer hinders leakage of gaseous DFP [26]). Coherently, in the same exposure conditions, the highest ADV yield is obtained in the case of DDAB-DexMA shell, that is more rigid than the DDAB one.

The elastic modulus of the DDAB shell is one order of magnitude higher than that of Epikouron™200-shelled systems [26] and those reported in literature for Sonovue® MBs [64]. This is consistent with a higher rigidity of DDAB, that at room temperature is organised in the gel-crystalline phase [48].

The vaporisation of AuNPs-decorated MDs was tested *via* both acoustic and optical stimulus. In the case of DDAB shell, preliminary tests reported in section S6 of ESI show that after vaporisation only few MBs remain stable in solution, due to shell breakage. Therefore, we focus our investigation on DDAB-DexMA-shelled MDs. As reported in Fig. 7, efficient ADV was obtained irradiating MDs for 5 min with an acoustic field of 520 mW/cm$^2$ intensity at 37 °C. DLS highlights that MDs successfully vaporise into stable MBs with diameter of 9.0 ± 0.9 μm (panel A). This is confirmed by CLSM experiments (panels B and C), where the core vaporisation is pointed out by the significant presence of larger particles mainly located close to the top interface with the glass slide and by the drop in the fluorescence intensity of Nile Red. These results remark the importance of the external crosslinked DexMA layer of the shell, which confers higher robustness to the system preventing the destabilisation of the DDAB layer when decorated by AuNPs [56]. Moreover, the elastomeric layer well withstands to the strong pressures arising from the enhancement and localisation of the acoustic field induced by AuNPs at the MDs interface [65].

The ODV experiments on AuNPs-decorated MDs are performed at 37 °C using a laser source at 532 nm with intensity of 34.0 ± 0.1 mW/cm$^2$. The irradiation time is selected at 120 s to maximise the vaporisation efficiency without inducing MDs burst (Fig. S20). DLS analysis (panel D of Fig. 7) highlights the successful vaporisation into MBs with diameter of 8.3 ± 0.9 μm. CLSM experiments on MDS labelled with Nile red (panels E and F of Fig. 7) confirm this result. Control experiments on non-decorated MDs reported in Fig. S21 show complete absence of vaporisation, demonstrating that the optical vaporisation occurs only in the presence of AuNPs adsorbed to the shell, and therefore the key role of the thermoplasmonic effect in converting into heat the incident energy.

It is interesting to compare the ODV process with the temperature-induced transition and rupture of MDs. To this aim, we carried out the UV-Visible extinction spectroscopy analyses reported in Fig. 8. Extinction spectra acquired on the AuNPs-decorated MDs before and after 3 min of laser irradiation are reported in panel A. The spectrum of bare AuNPs, showing the characteristic LSPR band centred at 534.5 ± 0.5 nm, is also reported for comparison. Before irradiation, the band is superimposed to the scattering contribution of MDs and appears weaker, broaden and redshifted to 539.5 ± 0.5 nm. This shift is due to the strong sensitivity of the LSPR to variations in the refractive index at the AuNPs surface [28,66]. Since dextran has higher refractive than water [67], this result ascertains the successful adsorption of AuNPs to the external layer of the MDs shell. After 3 min irradiation MDs break, as pointed out by DLS (Fig. S20). Accordingly, the scattering contribution of MDs vanishes in the extinction spectrum and the LSPR and the spectral shape becomes similar to that of bare AuNPs. The LSPR appears

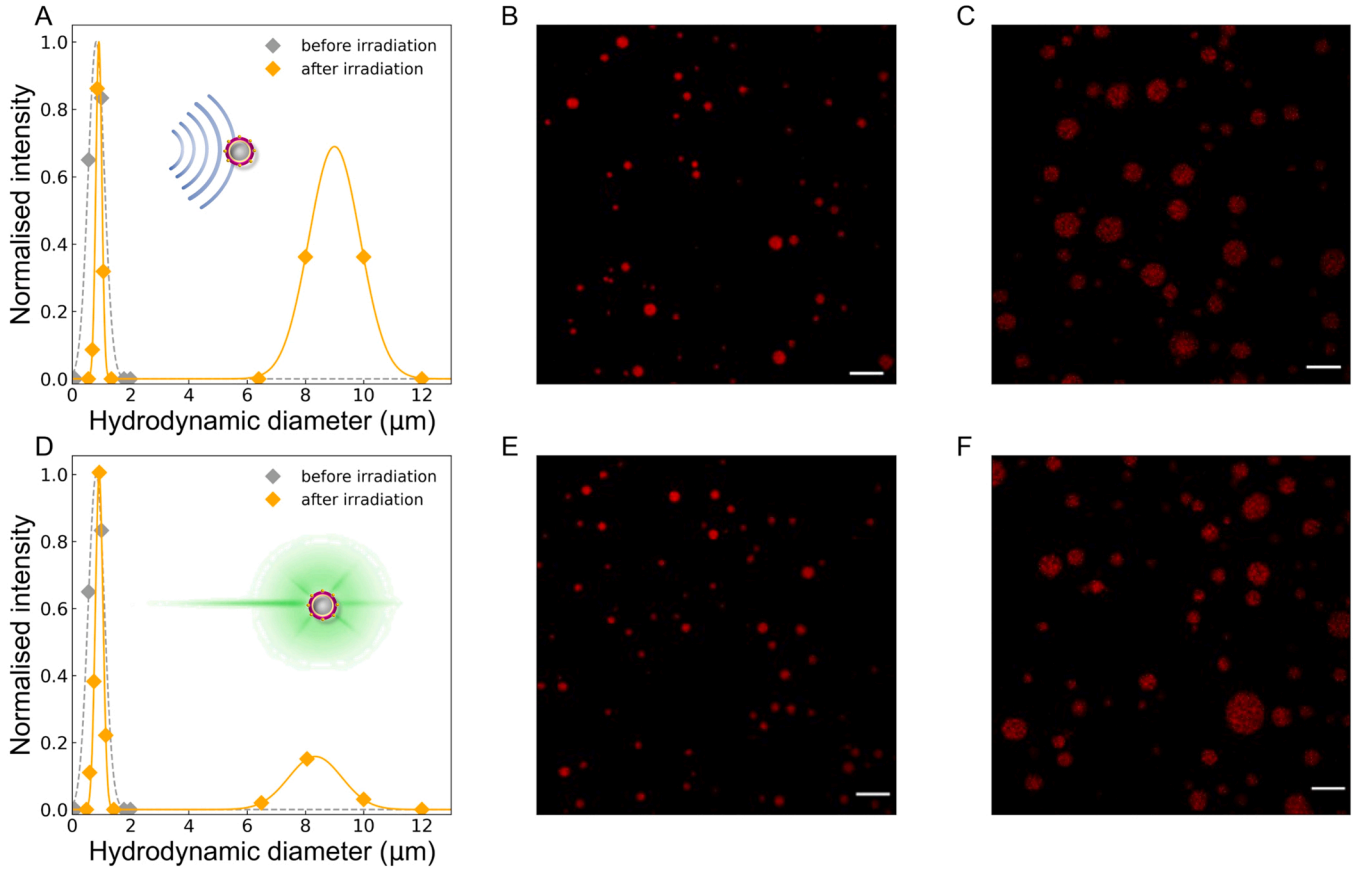


**Fig. 7.** DLS and CLSM study of acoustic and optical droplet vaporisation of AuNPs-decorated MDs with DDAB-DexMA shell. For ADV (top), MDs were exposed to an acoustic field of 520 mW/cm$^2$ intensity (peak negative pressure 120 kPa, mechanical index 0.12) for 5 min at 37 °C. Panel A shows the hydrodynamic diameter distributions measured before and after irradiation; corresponding CLSM images are reported in panels B and C, respectively. For ODV (bottom), MDs were exposed to laser illumination of 34 mW/cm$^2$ intensity for 120 s at 37 °C. Panel D shows the hydrodynamic diameter distributions measured before and after applying the optical stimulus; corresponding CLSM images are reported in panels E and F, respectively. Gaussian best fits of the size distributions are shown in the plots; scalebars are 10 μm.

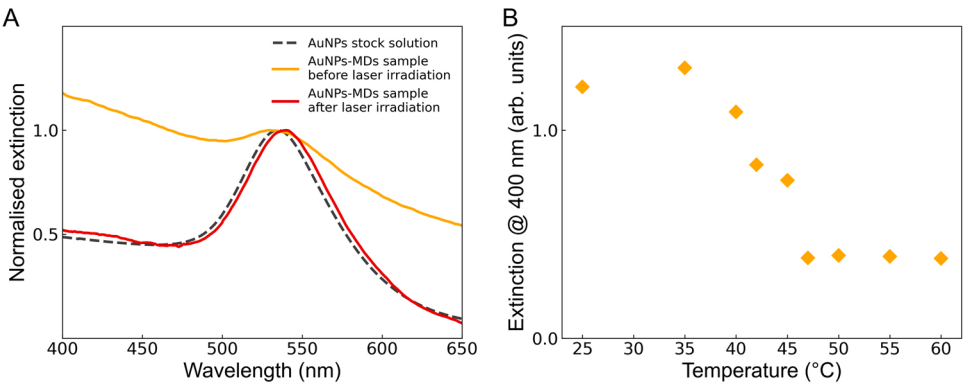


**Fig. 8.** (A) UV-Visible extinction spectra of AuNPs-decorated MDs with DDAB-DexMA shell before (orange) and after (red) laser stimulation (34 mW/cm$^2$, 3 min), compared with the plasmonic peak of free AuNPs (red); spectra are normalised to the maximum band intensity of the AuNPs LSPR. (B) Turbidimetric study of the ODV process: the measured values of the extinction at 400 nm are reported as a function of temperature. (For interpretation of the references to colour in this figure, the reader is referred to the web version of this article.)

further shifted to 543.5 ± 0.5 nm, suggesting that part of the shell components (DDAB and DexMA) adsorbs to AuNPs after MDs rupture.

The extinction spectra acquired as a function of temperature are reported in Fig. S15. To decouple the contribution of the MDs scattering to the extinction from the scattering and absorption of AuNPs, we report in panel B of Fig. 8 the extinction measured at 400 nm as a function of temperature. At this wavelength the contribution of AuNPs to the extinction is mainly due to inter-band transitions (*i.e.*, proportional to the molar concentration of Au in the sample) and therefore can be assumed constant for the overall temperature range [57]. The trend is characterised by an evident drop at ~45 °C, in correspondence of MDs rupture (see for comparison the DSC analyses of section S3).

The comparison between optically and temperature induced MDs burst highlights the possibility of exploiting the localised thermoplasmonic effect for the targeted release at physiological temperature of drugs or other agents previously embedded in MDs core. It is worth noting that the transition of the DDAB shell, that causes the MDs rupture, occurs well below the liquid-vapour transition temperature of the DFP core (increased from 55 °C to more than 70 °C when encapsulated within the double layer shell [26]). On the other hand, the optically induced vaporisation of MDs is mediated by AuNPs that are not directly in contact with the liquid core, meaning that an efficient heat transfer occurs thorough the DDAB-DexMA shell. This hypothesis is consistent if considering a shell thickness of ~300 nm [26] and an action distance for the heat transfer from plasmonic nanoparticles that can reach several hundred nanometres [68], while maintaining small the perturbed portion of the shell surface. This represents a promising asset of our system, in fact despite the easy synthesis procedure, the positioning of AuNPs at the external interface of the MDs shell, opens to their chemical derivatisation for targeting and efficient photothermal transfer against cancer cells [68].

## 4. Conclusions

In this work we developed two novel phase-change contrast agents using a single DDAB surfactant shell or double-layer shell made up of DDAB and crosslinked DexMA. Proceeding from the preparative previously developed for producing biodegradable phase-change contrast agents with hybrid interfaces [16], we modified and optimised the key parameters involved in the synthesis protocol to maximise the MDs stability against coalescence and rupture, and to select the best size distribution suitable for actual application of the produced MDs as ultrasound contrast agents or carriers. Specifically, we were able to achieve diameter distributions centred around 1.3 μm, suitable for reaching the smallest capillaries without inducing obstruction, with extremely narrow width, that ensures uniform acoustic response of the MBs formed after vaporisation of the MDs core. Moreover, the highly positive surface potential provided by DDAB ensures high colloidal stability to MDs. The structural stability and stiffness of the DDAB monolayer together with the elasticity of the polymer contribute to the high robustness of the DDAB-DexMA shelled MDs, which are still intact at physiological temperature and up to ~ 40 °C.

Our study results on the one hand in a novel formulation of robust DDAB-DexMA-shelled MDs with significant responsivity to ADV. The produced MBs resonate at the acoustic frequency of 15 MHz. The analysis of their acoustic response provided the characterisation of the viscoelastic properties of the two layers of the shell. Preliminary experiments on the obtained MBs showed very good echogenicity (see section S7 and Video S1) that makes our system interesting for designing novel contrast agents for echography imaging. On the other hand, the lower robustness of DDAB-shelled MDs may be employed for developing drug release strategies based on the acoustically triggered burst.

Supplementary material related to this article can be found online at doi:10.1016/j.colsurfa.2022.128522.

On this basis, we developed a multi-responsive system by decorating DDAB-DexMA-shelled MDs with AuNPs. The obtained hybrid system showed good stability and can be successfully vaporised by both acoustic and optical stimuli. These results open for promising application in combined biomedical approaches of theranostic relevance.

## CRediT authorship contribution statement

**Damiano Palmieri:** Collected the data, Performed the analysis, Writing – original draft, Writing – review & editing. **Francesco Brasili:** Collected the data, Performed the analysis, Writing – original draft, Writing – review & editing. **Angela Capocefalo:** Collected the data, Performed the analysis, Writing – original draft, Writing – review & editing. **Thomas Bizien:** Collected the data, Contributed data or analysis tools. **Ilaria Angelini:** Collected the data. **Letizia Oddo:** Collected the data, Supervision. **Yosra Toumia:** Collected the data, Supervision. **Gaio Paradossi:** Contributed data or analysis tools, Supervision. **Fabio Domenici:** Conceived and designed the analysis , Collected the data , Performed the analysis, Writing – original draft, Writing – review & editing, Supervision.

## Declaration of Competing Interest

The authors declare that they have no known competing financial interests or personal relationships that could have appeared to influence the work reported in this paper.

## Acknowledgements

Authors acknowledge SOLEIL for providing synchrotron radiation facilities under proposal n. 20180833 at the SWING beamline. The research leading to SAXS results has been supported by the project CALIPSOplus under the Grant Agreement 730872 from the EU Framework Programme for Research and Innovation Horizon 2020.

## Appendix A. Supporting information

Supplementary data associated with this article can be found in the online version at doi:10.1016/j.colsurfa.2022.128522.

## References


[1] M.A. Borden, G. Shakya, A. Upadhyay, K.H. Song, Acoustic nanodrops for biomedical applications, Curr. Opin. Colloid Interface Sci. 50 (2020), 101383, https://doi.org/10.1016/j.cocis.2020.08.008.

[2] O.D. Kripfgans, M.L. Fabiilli, P.L. Carson, J.B. Fowlkes, On the acoustic vaporization of micrometer-sized droplets, J. Acoust. Soc. Am. 116 (2004) 272–281, https://doi.org/10.1121/1.1755236.

[3] T. Si, G. Li, Q. Wu, Z. Zhu, X. Luo, R.X. Xu, Optical droplet vaporization of nanoparticle loaded stimuli-responsive microbubbles, Appl. Phys. Lett. 108 (2016), 111109, https://doi.org/10.1063/1.4944539.

[4] Y. Toumia, B. Cerroni, F. Domenici, H. Lange, L. Bianchi, M. Cociorb, F. Brasili, E. Chiessi, E. D'Agostino, K. Van Den Abeele, S.V. Heymans, J. D'Hooge, G. Paradossi, Phase change ultrasound contrast agents with a photopolymerized diacetylene shell, Langmuir 35 (31) (2019) 10116–10127, https://doi.org/10.1021/acs.langmuir.9b01160.

[5] Q. Chen, J. Yu, K. Kim, Review: optically-triggered phase-transition droplets for photoacoustic imaging, Biomed. Eng. Lett. 8 (2018) 223–229, https://doi.org/10.1007/s13534-018-0069-0.

[6] K. Loskutova, D. Grishenkov, M. Ghorbani, Review on acoustic droplet vaporization in ultrasound diagnostics and therapeutics, Hindawi BioMed. Res. Int. Vol. (2019), 9480193, https://doi.org/10.1155/2019/9480193 article ID 9480193.

[7] G. Calderó, G. Paradossi, Ultrasound/radiation-responsive emulsions, Curr. Opin. Colloid Interface Sci. 49 (2020) 118–132, https://doi.org/10.1016/j.cocis.2020.08.002.

[8] S. Lin, G. Zhang, A. Jamburidze, M. Chee, C.H. Leow, V. Garbin, M.-X. Tang, Imaging of vaporised sub-micron phase change contrast agents with high frame rate ultrasound and optics, Phys. Med. Biol. 63 (6) (2018), 065002, https://doi.org/10.1088/1361-6560/aaac05.

[9] M. Toulemonde, G. Zhang, R.J. Eckersley, M.-X. Tang. Flow Visualization through Locally Activated Nanodroplets and High Frame Rate Imaging. IEEE International Ultrasonics Symposium (IUS) 2018, 1–4 (2018). 10.1109/ULTSYM.2018.8579657.

[10] J.D. Dove, P.A. Mountford, T.W. Murray, M.A. Borden, Engineering optically triggered droplets for photoacoustic imaging and therapy, Biomed. Opt. Express 5 (12) (2014) 4417–4427, https://doi.org/10.1364/BOE.5.004417.

[11] K. Kooiman, S. Roovers, S.A. Langeveld, R.T. Kleven, H. Dewitte, M.A. O'Reilly, J.-M. Escoffre, A. Bouakaz, M.D. Verweij, K. Hynynen, I. Lentacker, E. Stride, C. K. Holland, Ultrasound-responsive cavitation nuclei for therapy and drug delivery, Ultrasound Med. Biol. 46 (6) (2020) 1296–1325.

[12] I. Beekers, M. Vegter, K.R. Lattwein, F. Mastik, R. Beurskens, A.F.W. van der Steen, N. de Jong, M.D. Verweij, K. Kooiman, Opening of endothelial cell–cell contacts due to sonoporation. J. Control. Release 322 (2020) 426–438, https://doi.org/10.1016/j.jconrel.2020.03.038.

[13] E. Tortorella, D. Palmieri, M. Piermarini, D. Gigante, L. Oddo, Y. Toumia, G. Paradossi, F. Domenici, Phase change dimethyldioctadecylammonium-shelled microdroplets as a promising drug delivery system: results on 3D Spheroids of mammalian tumor cells, J. Vis. Exp. 169 (2021), e62255, https://doi.org/10.3791/62255.

[14] R. Song, C. Peng, X. Xu, R. Zou, S. Yao, Facile fabrication of uniform nanoscale perfluorocarbon droplets as ultrasound contrast agents. Microfluid. Nanofluidics 23 (12) (2019) 1–10, https://doi.org/10.1007/s10404-018-2172-z.

[15] N. Vankova, S. Tcholakova, N.D. Denkov, I.B. Ivanov, V.D. Vulchev, T. Danner, Emulsification in turbulent flow: 1. Mean and maximum drop diameters in inertial and viscous regimes. J. Colloid Interface Sci. 312 (2) (2007) 363–380, https://doi.org/10.1016/j.jcis.2007.03.059.

[16] S. Capece, E. Chiessi, R. Cavalli, P. Giustetto, D. Grishenkov, G. Paradossi, A general strategy for obtaining biodegradable polymer shelled microbubbles as theranostic devices, Chem. Commun. 49 (51) (2013) 5763–5765, https://doi.org/10.1039/c3cc42037j.

[17] B. Cerroni, F. Righi Riva, L. Oddo, F. Domenici, E. Tortorella, Y. Toumia, F. Brasili, G. Paradossi, In vitro analysis of the trajectories of adhesive microbubbles approaching endothelial cells, J. Colloid Interface Sci. 578 (2020) 758–767, https://doi.org/10.1016/j.jcis.2020.06.009.

[18] L. Hoff, Acoustic Characterization of Contrast Agents for Medical Ultrasound Imaging, Springer Science & Business Media, 2001.

[19] F. Domenici, F. Brasili, L. Oddo, B. Cerroni, A. Bedini, F. Bordi, G. Paradossi, Long-term physical evolution of an elastomeric ultrasound contrast microbubble, J. Colloid Interface Sci. 540 (2019) 185, https://doi.org/10.1016/j.jcis.2018.12.110.

[20] A. Lawanprasert, A. Chau, J.N. Sloand, S. Hannifin, S.H. Medina, Tuning the interfacial properties of fluorous colloids toward ultrasound programmable bIoactivity, ACS Appl. Mater. Interfaces 13 (5) (2021) 5989–5998, https://doi.org/10.1021/acsami.0c20352.

[21] R. Chattaraj, G.M. Goldscheitter, A. Yildirim, A.P. Goodwin, Phase behavior of mixed lipid monolayers on perfluorocarbon nanoemulsions and its effect on acoustic contrast, RSC Adv. 6 (112) (2016) 111318–111325, https://doi.org/10.1039/C6RA20328K.

[22] F. Domenici, F. Brasili, S. Giantulli, B. Cerroni, A. Bedini, C. Giliberti, R. Palomba, I. Silvestri, S. Morrone, G. Paradossi, M. Mattei, F. Bordi, Differential effects on membrane permeability and viability of human keratinocyte cells undergoing very low intensity megasonic fields, Sci. Rep. 7 (16536) (2017), https://doi.org/10.1038/s41598-017-16708-4.

[23] S. Giantulli, E. Tortorella, F. Brasili, S. Scarpa, B. Cerroni, G. Paradossi, A. Bedini, S. Morrone, I. Silvestri, Fabio Domenici, Effect of 1-MHz Ultrasound on the proinflammatory Interleukin-6 secretion in human keratinocytes. Sci. Rep. 11 (19033) (2021) https://doi.org/10.1038/s41598-021-98141-2.

[24] S.R. Sirsi, M.A. Borden, State-of-the-art materials for ultrasound-triggered drug delivery, Adv. Drug Deliv. Rev. 72 (2014) 3–14, https://doi.org/10.1016/j.addr.2013.12.010.

[25] P.S. Sheeran, P.A. Dayton, Improving the performance of phase-change perfluorocarbon droplets for medical ultrasonography: current progress, challenges, and prospects, Scientifica 2014 (2014), 579684, https://doi.org/10.1155/2014/579684.

[26] S. Capece, F. Domenici, F. Brasili, L. Oddo, B. Cerroni, A. Bedini, F. Bordi, E. Chiessi, G. Paradossi, Complex interfaces in "phase-change" contrast agents, Phys. Chem. Chem. Phys. 18 (2016) 8378–8388, https://doi.org/10.1039/c5cp07538f.

[27] V. Amendola, R. Pilot, M. Frasconi, O.M. Maragò, M.A. Iatì, Surface plasmon resonance in gold nanoparticles: a review, J. Phys. Condens. Matter 29 (2017), 203002, https://doi.org/10.1088/1361-648X/aa60f3.

[28] A. Capocefalo, D. Mammucari, F. Brasili, C. Fasolato, F. Bordi, P. Postorino, F. Domenici, Exploring the potentiality of a SERS-active pH nano-biosensor, Front. Chem. 7 (2019) 413, https://doi.org/10.3389/fchem.2019.00413.

[29] C. Fasolato, S. Giantulli, A. Capocefalo, Y. Toumia, D. Notariello, F. Mazzarda, I. Silvestri, P. Postorino, F. Domenici, Antifolate SERS-active nanovectors: quantitative drug nanostructuring and selective cell targeting for effective theranostics, Nanoscale 11 (32) (2019) 15224–15233, https://doi.org/10.1039/C9NR01075K.

[30] A. Capocefalo, T. Deckert-Gaudig, F. Brasili, P. Postorino, V. Deckert, Unveiling the interaction of protein fibrils with gold nanoparticles by plasmon enhanced nano-spectroscopy, Nanoscale 13 (34) (2021) 14469, https://doi.org/10.1039/d1nr03190b.

[31] Z. Zhu, Q. Wu, G. Li, S. Han, T. Si, R.X. Xu, Microfluidic fabrication of stimuli-responsive microdroplets for acoustic and optical droplet vaporization, J. Mater. Chem. B 4 (2016) 2723–2730, https://doi.org/10.1039/c5tb02402a.

[32] W.-W. Liu, S.-H. Huang, P.-C. Li, Synchronized optical and acoustic droplet vaporization for effective sonoporation, Pharmaceutics 11 (279) (2019) 1–16, https://doi.org/10.3390/pharmaceutics11060279.

[33] K. Wilson, K. Homan, S. Emelianov, Biomedical photoacoustics beyond thermal expansion using triggered nanodroplet vaporization for contrast-enhanced imaging, Nat. Commun. 3 (618) (2012) 1–10, https://doi.org/10.1038/ncomms1627.

[34] X. Li, S. Zhong, C. Zhang, P. Li, H. Ran, Z. Wang, MAGE-targeted gold nanoparticles for ultrasound imaging-guided phototherapy in melanoma, BioMed. Res. Int. 2020 (2020), 6863231, https://doi.org/10.1155/2020/6863231.

[35] G. Baffou, F. Cichos, R. Quidant, Applications and challenges of thermoplasmonics, Nat. Mater. 19 (9) (2020) 946–958, https://doi.org/10.1038/s41563-020-0740-6.

[36] W. Li, X. Chen, Gold nanoparticles for photoacoustic imaging, Nanomedicine 10 (2) (2015) 299–320, https://doi.org/10.2217/nnm.14.169.

[37] J.B. Vines, J.-H. Yoon, N.-E. Ryu, D.-J. Lim, H. Park, Gold nanoparticles for photothermal cancer therapy, Front. Chem. 7 (2019) 167, https://doi.org/10.3389/fchem.2019.00167.

[38] H. Gao, Y. Bi, J. Chen, L. Peng, K. Wen, P. Ji, W. Ren, X. Li, N. Zhang, J. Gao, Z. Chai, Y. Hu, Near-infrared light-triggered switchable nanoparticles for targeted chemo/photothermal cancer therapy, ACS Appl. Mater. Interfaces 8 (24) (2016) 15103, https://doi.org/10.1021/acsami.6b03905.

[39] V.K. Sharma, H. Srinivasan, V. García Sakai, S. Mitra, Dioctadecyldimethylammonium bromide, a surfactant model for the cell membrane: Importance of microscopic dynamics, Struct. Dyn. 7 (5) (2020), 051301, https://doi.org/10.1063/4.0000030.

[40] J.N. Silva, A.C.N. Oliveira, M.P.P.A. Casal, A.C. Gomes, P.J. Coutinho, O. P. Coutinho, M.R. Oliveira, DODAB: monoolein-based lipoplexes as non-viral vectors for transfection of mammalian cells. Biochim. Et. Biophys. Acta (BBA) - Biomembr. 1808 (10) (2011) 2440, https://doi.org/10.1016/j.bbamem.2011.07.002.

[41] P. Callow, G. Fragneto, R. Cubitt, D.J. Barlow, M.J. Lawrence, P. Timmins, Interaction of cationic lipid vesicles with model cell membranes as determined by neutron reflectivity, Langmuir 21 (17) (2005) 7912, https://doi.org/10.1021/la050957l.

[42] M. Doucet, J.H. Cho, G. Alina, J. Bakker, W. Bouwman, P. Butler, K. Campbell, T. Cooper-Benun, C. Durniak, L. Forster, M. Gonzales, R. Heenan, A. Jackson, S. King, P. Kienzle, J. Krzywon, T. Nielsen, L. O'Driscoll, W. Potrzebowski, R. Ferraz Leal, P. Rozycko, T. Snow, A. Washington, SasView Version 5.0.0, Zenodo (2019), https://doi.org/10.5281/zenodo.3011184.

[43] S. Maaß, A. Gäbler, M. Wegener, A. Zaccone, A. Paschedag, M. Kraume, Experimental investigations and modelling of breakage phenomena in stirred liquid/liquid systems, Chem. Eng. Res. Des. 85 (5) (2007) 703–709, https://doi.org/10.1205/cherd06187.

[44] Y. Zhou, Application of acoustic droplet vaporization in ultrasound therapy, J. Ther. Ultrasound 3 (2015) 20, https://doi.org/10.1186/s40349-015-0041-8.

[45] A. Gäbler, M. Wegener, A.R. Paschedag, M. Kraume, The effect of ph on experimental and simulation results of transient drop size distributions in stirred

liquid-liquid dispersions, Chem. Eng. Sci. 61 (2006) 3018–3024, https://doi.org/10.1016/j.ces.2005.10.072.
[46] S. Ariyaprakai, K. Tananuwong, Freeze–thaw stability of edible oil-in-water emulsions stabilized by sucrose esters and Tweens, J. Food Eng. 152 (2015) 57–64, https://doi.org/10.1016/j.jfoodeng.2014.11.023.
[47] S. Fukushima, M. Takahashi, M. Yamaguchi, Effect of cetostearyl alcohol on stabilization of oil-in-water emulsion: I. Difference in the effect by mixing cetyl alcohol with stearyl alcohol, J. Colloid Interface Sci. 57 (2) (1976) 201–206, https://doi.org/10.1016/0021-9797(76)90193-4.
[48] F. Domenici, C. Castellano, F. Dell'Unto, A. Congiu, Temperature dependent structural changes on DDAB surfactant assemblies evidenced by energy dispersive X-ray diffraction and dynamic light scattering, Colloids Surf. B Biointerfaces 95 (2012) 170–177, https://doi.org/10.1016/j.colsurfb.2012.02.037.
[49] E. Feitosa, N.M. Bonassi, W. Loh, Vesicle-micelle transition in mixtures of dioctadecyldimethylammonium chloride and bromide with anonionic and zwitterionic surfactants, Langmuir 22 (10) (2006) 4512–4517, https://doi.org/10.1021/la052923j.
[50] D.J. Burgess, J.K. Yoon, Influence of interfacial properties on perfluorocarbon/aqueous emulsion stability, Colloids Surf. B: Biointerfaces 4 (1995) 297–308, https://doi.org/10.1016/0927-7765(94)01179-9.
[51] O. Shpak, M. Verweij, H.J. Vos, N. de Jong, D. Lohse, N. Versluis, Acoustic droplet vaporization is initiated by superharmonic focusing, Proc. Natl. Acad. Sci. 111 (5) (2014) 1697–1702, https://doi.org/10.1073/pnas.1312171111.
[52] G. Baffou, R. Quidant, Thermo-plasmonics: using metallic nanostructures as nano-sources of heat, Laser Photonics Rev. 7 (2) (2013) 171–187, https://doi.org/10.1002/lpor.201200003.
[53] Y.S. Chen, Y.C. Hung, I. Liau, G.S. Huang, Assessment of the in vivo toxicity of gold nanoparticles, Nanoscale Res. Lett. 4 (8) (2009) 858–864, https://doi.org/10.1007/s11671-009-9334-6.
[54] A. Guinier, G. Fournet, Small-Angle Scattering of X-Rays, John Wiley and Sons, New York, 1955.
[55] A. Bhat, L.W. Edwards, X. Fu, D.L. Badman, S. Huo, A.J. Jin, Q. Lu, Effects of gold nanoparticles on lipid packing and membrane pore formation, Appl. Phys. Lett. 109 (26) (2016), 263106, https://doi.org/10.1063/1.4972868.
[56] A. Schröder, J. Sprakel, K. Schroën, J.N. Spaen, C.C. Berton-Carabin, Coalescence stability of Pickering emulsions produced with lipid particles: a microfluidic study, J. Food Eng. 234 (2018) 63–72, https://doi.org/10.1016/j.jfoodeng.2018.04.007.
[57] F. Brasili, A. Capocefalo, D. Palmieri, F. Capitani, E. Chiessi, G. Paradossi, F. Bordi, F. Domenici, Assembling patchy plasmonic nanoparticles with aggregation-dependent antibacterial activity, J. Colloid Interface Sci. 580 (2020) 419–428, https://doi.org/10.1016/j.jcis.2020.07.006.
[58] D.S. Li, O.D. Kripfgans, M.L. Fabiilli, J. Brian Fowlkes, J.L. Bull, Initial nucleation site formation due to acoustic droplet vaporization, Appl. Phys. Lett. 104 (6) (2014), 063703, https://doi.org/10.1063/1.486411.
[59] S. Park, G. Son, Numerical investigation of acoustic vaporization threshold of microdroplets, Ultrason. Sonochem. 71 (2021), 105361, https://doi.org/10.1016/j.ultsonch.2020.105361.
[60] T. Lacour, M. Guédra, T. Valier-Brasier, F. Coulouvrat, A model for acoustic vaporization dynamics of a bubble/droplet system encapsulated within a hyperelastic shell, J. Acoust. Soc. Am. 143 (1) (2018) 23–37, https://doi.org/10.1121/1.5019467.
[61] M. Guédra, F. Coulouvrat, A model for acoustic vaporization of encapsulated droplets, J. Acoust. Soc. Am. 138 (6) (2015) 3656–3667, https://doi.org/10.1121/1.4937747.
[62] National Center for Biotechnology Information , 2021. PubChem Compound Summary for CID 86240, 1,1,1,2,2,3,4,5,5,5-Decafluoropentane. Retrieved February 19, 2021, from https://pubchem.ncbi.nlm.nih.gov/compound/2H_3H-Decafluoropentane.
[63] P. Marmottant, S. Van Der Meer, M. Emmer, M. Versluis, N. De Jong, S. Hilgenfeldt, D. Lohse, A model for large amplitude oscillations of coated bubbles accounting for buckling and rupture, J. Acoust. Soc. Am. 118 (6) (2005) 3499–3505, https://doi.org/10.1121/1.2109427.
[64] J. Tu, J. Guan, Y. Qiu, T.J. Matula, Estimating the shell parameters of SonoVue® microbubbles using light scattering, J. Acoust. Soc. Am. 126 (6) (2009) 2954–2962, https://doi.org/10.1121/1.3242346.
[65] G. Canavese, A. Ancona, L. Racca, M. Canta, M. Dumontel, F. Barbaresco, T. Limongi, V. Cauda, Nanoparticle-assisted ultrasound: a special focus on sonodynamic therapy against cancer, Chem. Eng. J. 340 (2018) 155–172, https://doi.org/10.1016/j.cej.2018.01.060.
[66] D. Caprara, F. Ripanti, A. Capocefalo, A. Sarra, F. Brasili, C. Petrillo, C. Fasolato, P. Postorino, DNA-functionalized gold nanoparticle assemblies for surface enhanced Raman scattering, Colloids Surf. A Physicochem. Eng. Asp. 589 (2020), 124399, https://doi.org/10.1016/j.colsurfa.2019.124399.
[67] J. Piehler, A. Brecht, K. Hehl, G. Gauglitz, Protein interactions in covalently attached dextran layers, Colloids Surf. B Biointerfaces 13 (6) (1999) 325–336, https://doi.org/10.1016/S0927-7765(99)00046-6.
[68] T. Grosges, D. Barchiesi, Gold nanoparticles as a photothermal agent in cancer therapy: the thermal ablation characteristic length, Molecules 23 (2018) 1316, https://doi.org/10.3390/molecules23061316.